J. Fluid Mech. (2009), *vol.* 622, *pp.* 115–134. © 2009 Cambridge University Press
doi:10.1017/S0022112008005120 Printed in the United Kingdom

Phase-field model for the Rayleigh–Taylor instability of immiscible fluids

ANTONIO CELANI[1], ANDREA MAZZINO[2],
PAOLO MURATORE-GINANNESCHI[3]
AND LARA VOZELLA[2,3]†

[1]Institut Pasteur, CNRS, URA 2171, 25 Rue du docteur Roux, 75015 Paris, France

[2]Department of Physics – University of Genova, and CNISM & INFN – Genova Section,
via Dodecaneso 33, 16146 Genova, Italy

[3]Department of Mathematics and Statistics – University of Helsinki, PO Box 4,
00014 Helsinki, Finland

(Received 3 June 2008 and in revised form 16 September 2008)

The Rayleigh–Taylor instability of two immiscible fluids in the limit of small Atwood numbers is studied by means of a phase-field description. In this method, the sharp fluid interface is replaced by a thin, yet finite, transition layer where the interfacial forces vary smoothly. This is achieved by introducing an order parameter (the phase-field) continuously varying across the interfacial layers and uniform in the bulk region. The phase-field model obeys a Cahn–Hilliard equation and is two-way coupled to the standard Navier–Stokes equations. Starting from this system of equations we have first performed a linear analysis from which we have analytically rederived the known gravity–capillary dispersion relation in the limit of vanishing mixing energy density and capillary width. We have performed numerical simulations and identified a region of parameters in which the known properties of the linear phase (both stable and unstable) are reproduced in a very accurate way. This has been done both in the case of negligible viscosity and in the case of non-zero viscosity. In the latter situation, only upper and lower bounds for the perturbation growth rate are known. Finally, we have also investigated the weakly nonlinear stage of the perturbation evolution and identified a regime characterized by a constant terminal velocity of bubbles/spikes. The measured value of the terminal velocity is in agreement with available theoretical prediction. The phase-field approach thus appears to be a valuable technique for the dynamical description of the stages where hydrodynamic turbulence and wave-turbulence come into play.

1. Introduction

The Rayleigh–Taylor (RT) instability is a fluid-mixing mechanism occurring at the interface of two fluids of different densities, subjected to an external acceleration. For a fluid in a gravitational field, such a mechanism was first discovered by Lord Rayleigh in the 1880s (Rayleigh 1883) and later applied to all accelerated fluids by G. I. Taylor (1950). The relevance of this mixing mechanism embraces many different phenomena occurring in completely different contexts. We just mention, among the many, astrophysical supernova explosions and geophysical formations such as salt

---

† Email address for correspondence: vozella@fisica.unige.it

domes and volcanic islands (Di Prima & Swinney 1981; Dimonte & Schneider 2000), continental magmatism caused by lithospheric gravitational instability (Ducea & Saleeby 1998; Lee, Rudnick & Brimhall Jr 2001), inertial confinement fusion (Cook & Zhou 2002) and cloud formation in atmospheric sciences (Schultz *et al.* 2006).

Back to classical fluids applications, RT instability is the first step, eventually leading to a fully developed turbulent regime. A deeper understanding of the mechanism of flows driven by RT instability thus would shed light on the many processes that underpin fully developed turbulence.

The difficulty inherent in sustaining an unstable density stratification has challenged experimentalists for over half a century. Several innovative approaches have been developed recently (see, e.g. Ramaprabhu & Andrews 2004).

With the advent of supercomputers, high-resolution numerical simulations of RT instability at high Reynolds numbers have become a reality. However, simulations using many different benchmark codes and experiments disagree already on apparently innocent observables such as, for instance, the value of the growth constant, α, associated to the spread of the turbulent mixing zone (see, e.g. Di Prima & Swinney 1981). The differences can be as high as 100 %.

Despite the long history of RT turbulence, a consistent phenomenological theory has been presented only recently (Chertkov 2003) for the miscible case. The theoretical predictions by Chertkov have been verified by Celani, Mazzino & Vozella (2006) exploiting numerical simulations in two spatial dimensions. For the three-dimensional miscible case we refer, for example, to Young *et al.* (2001).

In many of the aforementioned situations where the RT instability has an important role, the two fluids are immiscible owing to a non-negligible surface tension. At the level of linear analysis, the role played by a non-zero surface tension was addressed by Chandrasekhar (1961). The successive dynamics falling in a turbulent regime have been analysed by Chertkov, Kolokolov & Lebedev (2005). Using a phenomenological approach, the authors suggest the existence of a Kolmogorov cascade between the integral scale and a time-dependent scale related to the typical drop size. Below the latter scale, associated to an emulsion-like region, a wave energy cascade sets in. This is mediated by weakly interacting capillary waves propagating on top of the drop surface. Eventually, the energy is dissipated by viscous forces.

RT instability and RT turbulence of immiscible fluids thus appear richer than the corresponding miscible situations. The existence of two different cascades poses a serious challenge to numerical investigations of the immiscible RT problems. The emulsion-like phase occurs at very small scales and the energy transfer takes place on the interfaces. These are geometrical objects close to singularities and thus difficult to describe appropriately in a numerical scheme. Accuracy and efficiency are thus fundamental requirements to reproduce the correct statistical features characterizing immiscible RT turbulence.

Our aim here is to perform a first step along this direction by focusing on direct numerical simulations of immiscible RT instability. The numerical strategy we exploit here is known as phase-field model (Cahn & Hilliard 1958; Bray 2002; Badalassi, Ceniceros & Banerjee 2003; Ding, Spelt & Shu 2007). The main idea of the method is to treat the interface between two immiscible fluids as a thin mixing layer across which physical properties vary steeply but continuously. The evolution of the mixing layer is ruled by an order parameter (the phase-field) that obeys a Cahn–Hilliard equation (Cahn & Hilliard 1958). The method permits us to avoid a direct tracking of the interface and easily produces the correct interfacial tension from the mixing-layer free-energy.

The phase-field method differs with respect to other standard approaches where, for example, the interface between two immiscible fluids is modelled as a free boundary that evolves in time with the flow. The resulting equations of motions valid in each fluid domain are supplemented by boundary conditions at the free surface that involve the physical properties of the interface (see, for instance, Chandrasekhar 1961). Following this latter strategy, in order to handle the moving interface, a mesh with grid points on the interface which deforms according to the flow on both sides of the interface is commonly used. The main limitation of this approach is its inability to handle singular morphological changes such as breakup, coalescence and reconnections (see, Yue *et al.* 2004, and references therein). These dynamical features can be accurately described by the class of fixed-grid methods. According to this technique, the interface is smoothed, a fact that permitted us to obtain remarkable results for the quantitative description of deforming interfaces (for the level-set method see, e.g. Sethian 1999). Instead of describing the two fluids separately (with the appropriate boundary conditions), these methods represent the interfacial tension as a body force or bulk stress spread over a narrow region covering the interface. Then a single set of governing equations can be written over the entire domain and solved on a fixed grid in a purely Eulerian framework. The phase-field method belongs to this second class. It can be viewed as a physically motivated level-set method where instead of choosing an artificial smoothing function for the interface, which can affect the results in non-trivial ways (see Yue *et al.* 2004, and references therein), the description of the interface is suggested by physics via a mixing energy.

We present here an accurate numerical study that validates the phase-field approach by testing known results of immiscible RT instability at the level of both linear and weakly nonlinear analysis. From our results, it turns out that this strategy is a valuable option for a quantitative treatment of the turbulent regime characterized by the interplay between hydrodynamic and interface degrees of freedom.

The paper is organized as follows. In § 2, we introduce the Rayleigh–Taylor problem and discuss the related phase-field approach. A detailed analysis of the energy balance between purely hydrodynamic degrees of freedom and interface degrees of freedom is presented. Finally, the dispersion relation for gravity–capillary waves is obtained by analytical calculations starting from the phase-field equation coupled to the Navier–Stokes equations. In § 3, the results from the direct numerical simulations are presented and compared with known results for the linear analysis. We focus both on the case of zero viscosity and on that of non-negligible viscosity. Both stable and unstable configurations are considered. Finally, the weakly nonlinear regime is considered and the resulting terminal velocity of bubbles/spikes compared with existing theoretical predictions. Section 4 is devoted to some conclusions and perspectives. Appendices A, B and C collect supplementary information not contained in the main text.

2. System configuration and phase-field model

Our system consists of two immiscible incompressible fluids (labelled 1 and 2) having different densities, ρ_1 and $\rho_2 > \rho_1$, with the denser fluid placed above the less dense one (see figure 1). In the absence of gravity, this flow configuration is stable. In the presence of the gravitational force, surface tension may be able to keep the system in equilibrium, provided the density contrast is not too large.

Let us start by describing the equilibrium configuration and then pass to the evolution (RT instability) that occurs when a perturbation is imposed on the interface separating the two fluids.

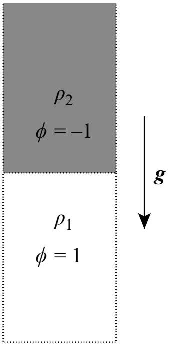

FIGURE 1. Fluids configuration corresponding to a heavier fluid of density ρ_2 placed above a lighter one of density $\rho_1 < \rho_2$.

2.1. *Equilibrium state*

Let us consider an equilibrium state where fluid 1 is placed below fluid 2 and they are separated by a sharp interface. The fact that the interface is sharp (i.e. a discontinuity in the fluid properties) poses a serious challenge to numerical simulations. For sharp interfaces, the evolution equations are obtained by following fluids 1 and 2 separately with the appropriate boundary condition at the interface (see, for instance, Sethian 1999; Smolianski, Haario & Luukka 2005). Other approaches follow the interface alone. In this latter case, the movement of the interface is naturally amenable to a Lagrangian description, while the bulk flow is conventionally solved in an Eulerian framework. These approaches employ a mesh that has grid points on the interfaces and deforms according to the flow. A major shortcoming of these approaches is that they cannot handle properly topological changes such as breakup, coalescence and reconnections (see Yue *et al.* 2004, and references therein). In this respect, the phase-field method is, by far and away, more effective, at the expense of a larger number of grid points required.

The idea of the phase-field method is to replace the sharp interface with a diffuse one in such a way that the numerical computation of interface movement and deformation can be carried out on fixed grids (Anderson, McFadden & Wheeler 1998; Jacqmin 1999). More quantitatively, this amounts to assigning to the system a Ginzburg–Landau free-energy, $\mathscr{F}$, expressed in term of the order parameter ϕ as (Cahn & Hilliard 1958; Bray 2002; Yue *et al.* 2004):

$$\mathscr{F}[\phi] = \int_{\Omega} \frac{\Lambda}{2}|\boldsymbol{\partial}\phi(\boldsymbol{x})|^2 + \frac{\Lambda}{4\epsilon^2}(\phi^2 - 1)^2 \, \mathrm{d}\boldsymbol{x}, \tag{2.1}$$

where Ω is the region of space occupied by the system, $\boldsymbol{\partial} \equiv \partial_i$ with $i = 1, \ldots, d$, d being the space dimensions and ϵ is the capillary width, representative of the interface thickness. In the following, we refer to $\Lambda[|\boldsymbol{\partial}\phi(\boldsymbol{x})|^2/2 + (\phi^2 - 1)^2/(4\epsilon^2)]$ as a density of free-energy and to Λ as the magnitude of the free energy. The order parameter ϕ is a field which serves to identify fluid 1 and 2. We assume $\phi = 1$ in the region occupied by fluid 1 and $\phi = -1$ in those where fluid 2 is present.

The equilibrium state is the minimizer of the free-energy $\mathscr{F}$. The mechanism which keeps the system in this configuration is the competition between two effects due to the two addends in (2.1). The first term favours a mixing (i.e. $\Lambda|\boldsymbol{\partial}\phi|^2/2 = 0$ in $\mathscr{F}$, this term being the interface energy contribution) whereas the second one drives the system towards demixing (the associated term in $\mathscr{F}$, the bulk contribution, has a minimum for $\phi = \pm 1$). The non-trivial final equilibrium state is merely the results of this competition. More quantitatively, the final state is obtained by minimizing the free-energy functional with respect to variations of the function ϕ, i.e. solving:

$$\mu \equiv \delta \mathscr{F}/\delta\phi = 0 \Leftrightarrow -\partial^2\phi + \frac{\phi^3 - \phi}{\epsilon^2} = 0, \tag{2.2}$$

where μ is the so-called chemical potential (see, for instance, Cahn & Hilliard 1958; Bray 2002; Yue *et al.* 2004). If we consider a one-dimensional interface, varying along the gravitational direction y, we easily find the solution of (2.2) as (Cahn & Hilliard 1958; Bray 2002; Yue *et al.* 2004):

$$\phi(y) = \pm \tanh\left(\frac{y}{\sqrt{2}\epsilon}\right). \tag{2.3}$$

From (2.3), we immediately realizes that the sharp-interface limit is obtained for $\epsilon \to 0$: in this case $\tanh(y/(\sqrt{2}\epsilon)) \to \mathrm{sign}(y)$. Moreover, the surface tension σ is equal to the integral of the free-energy density along the interface (see, for example, Landau & Lifshitz 2000). For a plane interface, this integral yields (Cahn & Hilliard 1958; Bray 2002; Yue *et al.* 2004):

$$\sigma = \frac{2\sqrt{2}}{3}\frac{\Lambda}{\epsilon}. \tag{2.4}$$

It is now easy to verify how the sharp-interface limit is obtained: it suffices to take the limits Λ and ϵ to zero, keeping σ fixed to the value prescribed by surface tension (Liu & Shen 2003).

2.2. *Perturbation evolution*

Let us now suppose that we impose a small perturbation on the (finite thickness) interface separating the two fluids. Such a perturbation will displace the phase field from the previous equilibrium configuration, which minimized the free energy $\mathscr{F}$, to a new configuration for which in general, $\mu \neq 0$. The system will react so as to try to reach again an equilibrium configuration. This can be expressed as,

$$\frac{\partial\phi}{\partial t} + \boldsymbol{v}\cdot\boldsymbol{\partial}\phi = \gamma\partial^2\mu = \gamma\,\Lambda\partial^2\left[-\partial^2\phi + \frac{(\phi^3-\phi)}{\epsilon^2}\right], \tag{2.5}$$

γ being the so-called mobility (see, for instance, Bray 2002; Yue *et al.* 2004). Notice the presence of the Laplacian operator in front of μ which causes the mass of each fluid to be conserved, as imposed by the physics of the problem under consideration.

The dynamics of the velocity field is governed by the usual Boussinesq Navier–Stokes equations (Kundu & Cohen 2001) plus an additional stress contribution arising at the interface where the effect of surface tension enters into play (Bray 2002; Yue *et al.* 2004; Berti *et al.* 2005). The equations of motion are:

$$(\partial_t v_i + \boldsymbol{v}\cdot\boldsymbol{\partial}v_i) = -\frac{\partial_i p}{\rho_o} + \nu\partial^2 v_i - \frac{\phi}{\rho_o}\partial_i\frac{\delta\mathscr{F}}{\delta\phi} + \frac{\rho'}{\rho_o}g_i, \tag{2.6}$$

$$\boldsymbol{\partial}\cdot\boldsymbol{v} = 0. \tag{2.7}$$

In (2.6), $\rho_o = (\rho_1 + \rho_2)/2$, ν is the kinematic viscosity and $\boldsymbol{g}$ is the acceleration due to gravity. For the sake of notation we will denote derivatives and velocity (e.g. for $d = 3$) as $\boldsymbol{\partial} \equiv (\partial_1, \partial_2, \partial_3) = (\partial_x, \partial_y, \partial_z)$ and $\boldsymbol{v} \equiv (v_1, v_2, v_3) = (u, v, w)$, respectively. The quantity $-\phi\boldsymbol{\partial}(\delta\mathscr{F}/\delta\phi)/\rho_o$ is the coupling term that accounts for capillary forces. It is easy to verify that it can be rewritten as $-\Lambda(\partial^2\phi\boldsymbol{\partial}\phi)/\rho_o$ plus a gradient term which can be absorbed into the pressure term. Finally, $\rho' g_i/\rho_o$ is the buoyancy contribution, ρ' being the deviation of the actual density, ρ, from the mean density ρ_o:

$$\rho' = \rho - \rho_o.$$

The buoyancy contribution can be rewritten in terms of ρ_1, ρ_2 and ϕ as:

$$\begin{aligned} \frac{\rho'}{\rho_o} g_i &= \frac{\rho - \rho_o}{\rho_o} g_i \\ &= \frac{\rho_1((1+\phi)/2) + \rho_2((1-\phi)/2) - \rho_o}{\rho_o} g_i \\ &= -\mathscr{A}\phi\, g_i, \end{aligned} \tag{2.8}$$

where $\mathscr{A} \equiv (\rho_2 - \rho_1)/(\rho_2 + \rho_1)$ is the Atwood number.

2.3. *Energetics*

Let us define the kinetic energy (per unit volume), E_K, and the potential energy (per unit volume), E_P, for our system ruled by (2.5), (2.6) and (2.7).

By definition of potential energy, we have:

$$\begin{aligned} E_P &= \frac{1}{\Omega}\int\!\!\int \mathrm{d}x\,\mathrm{d}y\,\rho_2\, g\, y\frac{1-\phi}{2} + \frac{1}{\Omega}\int\!\!\int \mathrm{d}x\,\mathrm{d}y\,\rho_1\, g\, y\frac{1+\phi}{2} + E_P^o \\ &= -\tfrac{1}{2}\langle y\,\phi\rangle(\rho_2 - \rho_1)g = -\rho_o\,\mathscr{A}\, g\,\langle y\,\phi\rangle, \end{aligned} \tag{2.9}$$

Ω being the total volume occupied by the fluids, and angle brackets, denote spatial averages. In (2.9), the constant E_P^o is chosen such as to set the potential energy to zero for vanishing Atwood number.

In a similar way, we can define the kinetic energy per unit volume as:

$$\begin{aligned} E_K &= \frac{1}{\Omega}\int\!\!\int \mathrm{d}x\,\mathrm{d}y\,\rho_2\,\frac{1-\phi}{2}\,\frac{\boldsymbol{v}^2}{2} + \frac{1}{\Omega}\int\!\!\int \mathrm{d}x\,\mathrm{d}y\,\rho_1\,\frac{1+\phi}{2}\,\frac{\boldsymbol{v}^2}{2} \\ &= \rho_2\left\langle\left(\frac{1-\phi}{2}\right)\frac{\boldsymbol{v}^2}{2}\right\rangle + \rho_1\left\langle\left(\frac{1+\phi}{2}\right)\frac{\boldsymbol{v}^2}{2}\right\rangle \\ &= \rho_o\left\langle\frac{\boldsymbol{v}^2}{2}\right\rangle - \rho_o\,\mathscr{A}\left\langle\phi\,\frac{\boldsymbol{v}^2}{2}\right\rangle. \end{aligned} \tag{2.10}$$

From (2.5) and (2.6), we immediately realize that such equations are left invariant under the simultaneous transformation $\boldsymbol{g} \to -\boldsymbol{g}$, $\phi \to -\phi$. As a consequence, $\langle\phi\,\boldsymbol{v}^2/2\rangle = 0$, and the resulting kinetic energy is simply:

$$E_K = \rho_o\,\langle\boldsymbol{v}^2/2\rangle. \tag{2.11}$$

By defining $E_{\mathscr{F}} \equiv \mathscr{F}/\Omega$, the total energy of the two-fluid system is

$$E = E_P + E_K + E_{\mathscr{F}}.$$

The equation for E_K is obtained by multiplying (2.6) by $\rho_o v_i$ and then taking the spatial average. We easily obtain:

$$\mathrm{d}E_K/\mathrm{d}t = \rho_o\partial_t\langle\boldsymbol{v}^2/2\rangle = -\rho_o\nu\langle(\partial_i\,\boldsymbol{v})^2\rangle + \rho_o\,\mathscr{A}\,g\langle v\phi\rangle - \Lambda\langle v_i\,(\partial_i\phi)\,(\partial^2\phi)\rangle. \tag{2.12}$$

Let us now take (2.5), multiply it by y, and take the average. Exploiting translational invariance and the Leibniz rule, the following equation can be easily obtained

$$\partial_t\langle y\,\phi\rangle + \langle y\,\partial_y\,(v\phi)\rangle = \gamma\Lambda\left\langle y\,\partial^2\left(-\partial^2\phi + \frac{\phi^3 - \phi}{\epsilon^2}\right)\right\rangle = 0. \tag{2.13}$$

We thus have:

$$\mathrm{d}E_P/\mathrm{d}t = -\partial_t(\rho_o \mathscr{A} g\langle y\,\phi\rangle) \;= -\,\rho_o \mathscr{A} g\langle v\phi\rangle, \tag{2.14}$$

where we have used the fact that $\langle y\partial_y(v\phi)\rangle = -\,\langle(\partial_y y)v\phi\rangle = -\,\langle v\phi\rangle$. The free-energy variation is:

$$\begin{aligned}
\partial_t\mathscr{F} &= \int\!\!\int \frac{\delta\mathscr{F}}{\delta\phi}\frac{\partial\phi}{\partial t}\,\mathrm{d}x\,\mathrm{d}y \\
&= \int\!\!\int \frac{\delta\mathscr{F}}{\delta\phi}\left[-\boldsymbol{v}\cdot\boldsymbol{\partial}\phi + \gamma\partial^2\left(\frac{\delta\mathscr{F}}{\delta\phi}\right)\right]\mathrm{d}x\,\mathrm{d}y \\
&= -\gamma\left\langle\left[\partial\left(\frac{\delta\mathscr{F}}{\delta\phi}\right)\right]^2\right\rangle\Omega - \int\!\!\int\left(\frac{\delta\mathscr{F}}{\delta\phi}\right)v_i\partial_i\phi\,\mathrm{d}x\,\mathrm{d}y \\
&= -\gamma\left\langle\left[\partial\left(\frac{\delta\mathscr{F}}{\delta\phi}\right)\right]^2\right\rangle\Omega - \Lambda\int\!\!\int\left[(-\partial^2\phi) + \frac{\phi^3-\phi}{\epsilon^2}\right]v_i\partial_i\phi\,\mathrm{d}x\,\mathrm{d}y \\
&= -\gamma\left\langle\left[\partial\left(\frac{\delta\mathscr{F}}{\delta\phi}\right)\right]^2\right\rangle\Omega - \Lambda\langle e_{ij}(\partial_i\phi)(\partial_j\phi)\rangle\Omega.
\end{aligned} \tag{2.15}$$

that is,

$$\partial_t E_{\mathscr{F}} \;=\; -\gamma\left\langle\left[\partial_i\left(\frac{\delta\mathscr{F}}{\delta\phi}\right)\right]^2\right\rangle \;-\; \Lambda\langle e_{ij}\,(\partial_i\phi)\,(\partial_j\phi)\rangle, \tag{2.16}$$

where we have introduced the strain tensor $e_{ij} \equiv \left(\partial_i v_j + \partial_j v_i\right)/2$ and assumed boundary conditions suitable for justifying integrations by parts.

The energy balance takes then the form:

$$\partial_t(E_K \;+\; E_P \;+\; E_{\mathscr{F}}) \;=\; -\rho_o\nu\langle(\partial_i\boldsymbol{v})^2\rangle - \gamma\left\langle\left[\partial_i\left(\frac{\delta\mathscr{F}}{\delta\phi}\right)\right]^2\right\rangle. \tag{2.17}$$

The global system is thus essentially dissipative, even for a vanishing kinetic viscosity. It is worth emphasizing the cancellation of $\Lambda\langle e_{ij}(\partial_i\phi)(\partial_j\phi)\rangle$ by the kinetic and the free-energy contributions, owing to exchanges between the velocity field and the interface.

2.4. *Dispersion relation for the phase-field model*

The aim of this section is to show that the well-known dispersion relation for gravity–capillary waves (Chandrasekhar 1961) can be easily obtained within the phase-field formalism. To do that, let us concentrate our attention on a two-dimensional problem and indicate the gravity direction by y. Moreover, we will assume the heavier fluid to be placed below the lighter one, in such a way as to have a stable situation. For a given perturbation imposed to the interface, the problem is to determine how the perturbation evolves in time.

Denoting by $h(x,t)$ a small perturbation imposed on a planar interface, we can rewrite ϕ as:

$$\phi = f\left(\frac{y-h(x,t)}{\epsilon}\right), \tag{2.18}$$

where h can be larger than ϵ, yet it must be smaller than the scale of variation of h (small amplitudes).

From the local equilibrium of the interface, the following equation for:

$$q_y \equiv \lim_{L\uparrow\infty} \int_{-L}^{L} v \,\mathrm{d}y, \tag{2.19}$$

is easily obtained (see Appendix A):

$$\rho_o \partial_t q_y = \sigma \frac{\partial^2 h}{\partial x^2} - 2\mathscr{A} g \rho_o h. \tag{2.20}$$

The height variation of the interface has to match the vertical fluid velocity, thus giving:

$$\partial_t h = v(x, h(x,t), t) \equiv v^{(int)}(x,t). \tag{2.21}$$

The last step is to relate the velocity at the interface with the integral q_y. This is done by restricting ourselves to potential flows. The final result in Fourier space is (see Appendix A):

$$\hat{v}^{(int)} = \tfrac{1}{2} k \hat{q}_y. \tag{2.22}$$

By solving (2.21) and (2.22), we obtain,

$$\partial_t^2 \hat{h} + \omega^2 \hat{h} = 0, \tag{2.23}$$

with

$$\omega^2(k) = \mathscr{A} g k + \frac{\sigma}{2\rho_o} k^3, \tag{2.24}$$

which is the expected dispersion relation (Chandrasekhar 1961). For the stable configuration we have, for all values of σ: $\mathscr{A} g k + \sigma/(2\rho_o) k^3 > 0$, i.e. any initially imposed perturbation will not grow indefinitely.

From (2.23) and the initial condition:

$$\partial_t \hat{h}(k,t) = 0 \quad \text{at } t = 0, \tag{2.25}$$

we immediately have:

$$\hat{h}(k,t) = \hat{h}(k,0)\cos(\omega t), \tag{2.26}$$

and the velocity at the interface reads:

$$\hat{v}_y^{int}(k,t) = -\hat{h}(k,0)\omega \sin(\omega t). \tag{2.27}$$

Assuming an initial perturbation of the form $h(x,0) = h_0 \cos(\bar{k}x)$ from (A 14) and (2.27) we obtain:

$$\hat{\psi}(\bar{k},t) = \frac{1}{\bar{k}} \hat{h}(\bar{k},0)\omega \sin(\omega t), \tag{2.28}$$

and the velocity components, for $y > 0$:

$$v^{\uparrow}(x,y,t) \equiv v(x,y,t) = -\cos(\bar{k}x) e^{-\bar{k}y} h_o \omega \sin(\omega t), \tag{2.29}$$

$$u^{\uparrow}(x,y,t) \equiv u(x,y,t) = \sin(\bar{k}x) e^{-\bar{k}y} h_o \omega \sin(\omega t), \tag{2.30}$$

where we used the relation $h_0 = 2\hat{h}(k,0)$.

For $y < 0$, in a similar way, we obtain the velocity field components:

$$v^{\downarrow}(x,y,t) \equiv v(x,y,t) = -\cos(\bar{k}x) e^{+\bar{k}y} h_o \omega \sin(\omega t), \tag{2.31}$$

$$u^{\downarrow}(x,y,t) \equiv u(x,y,t) = -\sin(\bar{k}x) e^{+\bar{k}y} h_o \omega \sin(\omega t). \tag{2.32}$$

When in the initial configuration the heavier fluid is placed above the lighter one, the dispersion relation (2.24) transforms into:

$$\omega^2(\bar{k}) = -\mathscr{A} g\bar{k} + \frac{\sigma}{2\rho_o}\bar{k}^3, \tag{2.33}$$

which is readily obtained by flipping the sign of g. For $\sigma < \sigma_c \equiv 2\rho_o/(\mathscr{A} g\bar{k}^2)$, surface tension is not able to contrast gravity-induced vertical motion, with the final result that amplitude perturbations grow exponentially: the flow is unstable. More precisely, from (2.33) and for $\sigma < \sigma_c$, we have:

$$\omega(\bar{k}) = \sqrt{-\mathscr{A} g\bar{k} + \frac{\sigma}{2\rho_o}\bar{k}^3} \equiv \mathrm{i}\,\alpha(\bar{k}), \tag{2.34}$$

and (2.29)–(2.32) transform into:

$$v^{\uparrow}(x,y,t) \equiv v(x,y,t) = \cos(\bar{k}x)\mathrm{e}^{-\bar{k}y} h_0\alpha \sinh(\alpha t), \tag{2.35}$$

$$u^{\uparrow}(x,y,t) \equiv u(x,y,t) = -\sin(\bar{k}x)\mathrm{e}^{-\bar{k}y} h_0\alpha \sinh(\alpha t), \tag{2.36}$$

for $y > 0$, and:

$$v^{\downarrow}(x,y,t) \equiv v(x,y,t) = \cos(\bar{k}x)\mathrm{e}^{+\bar{k}y} h_0\alpha \sinh(\alpha t), \tag{2.37}$$

$$u^{\downarrow}(x,y,t) \equiv u(x,y,t) = \sin(\bar{k}x)\mathrm{e}^{+\bar{k}y} h_0\alpha \sinh(\alpha t), \tag{2.38}$$

for $y < 0$.

3. Numerical investigation

In this section, we report results we have obtained by exploiting direct numerical simulations (DNS) of the phase-field model for the Rayleigh–Taylor problem described in the preceding sections. We will focus both on the linear phase of the perturbation evolution and on the weakly nonlinear regime governed by plumes, for $\mathscr{A} \ll 1$.

In the present study, we will consider initial perturbations imposed on the interface varying along one of the horizontal directions, say the x-axis, and invariant along the other horizontal direction, say the z-axis. The perturbation is thus essentially two-dimensional, a fact that allows us to solve the original Navier–Stokes equations coupled to the phase field in two dimensions. This clearly permits us to obtain high accuracy and thus to properly test the phase-field approach against known results for both the linear and the nonlinear evolution stage.

For a two-dimensional flow, it is convenient to introduce the vorticity field ω $[\omega = (\boldsymbol{\partial} \times \boldsymbol{v})_z]$ and study the equations:

$$\partial_t\omega + \boldsymbol{v}\cdot\boldsymbol{\partial}\omega = \nu\partial^2\omega - \frac{\Lambda}{\rho_o}\boldsymbol{\partial} \times (\partial^2\phi\,\boldsymbol{\partial}\phi) - \mathscr{A}(\boldsymbol{\partial}\phi)\times\boldsymbol{g}, \tag{3.1}$$

$$\partial_t\phi + \boldsymbol{v}\cdot\boldsymbol{\partial}\phi = \gamma\partial^2\mu = \gamma\,\Lambda\partial^2\left[-\partial^2\phi + \frac{(\phi^3-\phi)}{\epsilon^2}\right]. \tag{3.2}$$

In order to solve those equations efficiently and accurately, we exploit a pseudospectral method. Accordingly, periodic boundary conditions have to be assumed along the two directions. For the horizontal direction it is a natural choice (see e.g. Liu & Shen 2003; Cabot & Cook 2006), while along the vertical direction this choice deserves some comments. As the initial condition, we started from the hyperbolic-tangent profile, (2.3), for ϕ with the interface placed in the middle of the domain. The fact that we have periodic boundary conditions along y simply means that far from the middle of the domain, the hyperbolic-tangent profile has to be distorted in order to satisfy periodic boundary conditions. However, both in the linear and in the weakly nonlinear regimes, the amplitude of the interface perturbation is always much smaller than the vertical size of the box, so that the actual choice of boundary conditions at the top and bottom can be safely neglected. Periodic boundary conditions along the vertical have already been exploited for the miscible case by Celani *et al.* (2006). More quantitatively, as the perturbation grows, here we use the empirical criterion, according to which the ratio of bubble/spike height to the vertical dimension of the domain is always smaller than ~ 0.2. Test cases with smaller ratios do not produce appreciable differences in the results we are going to discuss (for the weakly nonlinear case see figure 7).

The box has a horizontal to vertical aspect ratio $L_x/L_y = 1$ for the linear analysis stage and $L_x/L_y = 1/2$ for the weakly nonlinear evolution ($L_x/L_y = 1/4$ for the test case reported in figure 7). In the weakly nonlinear case, we take a smaller aspect ratio because the perturbation can reach a higher amplitude (with respect to the case of the linear analysis).

As far as the resolution is concerned, it is 1024×1024 collocation points for the case $L_x/L_y = 1$ and 1024×2048 for $L_x/L_y = 1/2$. We need such a high resolution (despite the fact that we focus on a linear and weakly nonlinear study) in order to have a well-described interface separating the two phases. In our simulations, the mixing width ($\sim 4\epsilon$) is 6 mesh points.

The time evolution is implemented by a standard second-order Runge–Kutta scheme.

The physically relevant parameters in the present problem are the kinematic viscosity ν, the buoyancy intensity $\mathscr{A}g$, and the surface tension σ. Both $\mathscr{A}g$ and ν will be varied in our study, while σ will be kept to a fixed value (see below). The surface tension is related to the ratio Λ/ϵ with ϵ (and thus Λ) sufficiently small in order to have a finite value for the surface tension and, at the same time, to reproduce the correct sharp-interface limit. Finally, the parameter γ appearing in the relaxation term in (3.2) must satisfy the requirement that $\gamma\Lambda$ be small, so as to enforce 'instantaneous' local equilibrium between flow and interface. Here, we used the value (model units) $\gamma\Lambda = 10^{-8}$.

All simulations presented here start from an initial condition corresponding to an equilibrium configuration: velocity identically zero and hyperbolic tangent profile for the phase-field ϕ, expressed by the relation of the form: $\tanh((y - h(x, t = 0))/\sqrt{2}\epsilon)$ with

$$h(x, \mathrm{t} = 0) = h_0 \sin(k\,x).$$

For a given k, we choose the initial amplitude h_0 in such a way that h_0/λ (where $\lambda \equiv 2\pi/k$) is sufficiently small to fall in the linear phase (i.e. $h_0/\lambda \ll 1$) and h_0 is sufficiently large for the wave disturbance to see an almost infinitesimal mixing width (i.e. $h_0/\epsilon \gg 1$). Specific numerical values are reported in the following sections.

3.1. *Linear instability for negligible viscosity*

The aim of this section is to verify the growth rate (2.34) which holds in the linear phase when the viscosity is negligible.

In order to do so, we take a small value of ν ($\nu = 10^{-5}$ in the model units) and vary k (up to $k_c \equiv (2\mathscr{A}g\rho_o/\sigma)^{1/2}$, the critical wavenumber separating unstable from stable wave modes) and Ag, and take a fixed value of σ. The ratio $h_0/\lambda = 0.06$, while h_0/ϵ ranges from ~ 10 to ~ 40 in the range of k considered.

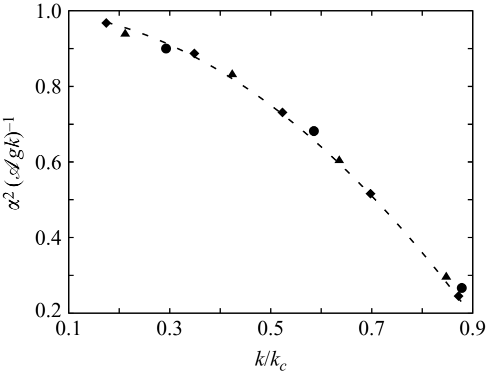

FIGURE 2. The squared growth rate α^2 (see (2.34)) for three different values of $\mathscr{A}g$ corresponding to three different values of the critical wavenumber $k_c \equiv (2\mathscr{A}g\rho_o/\sigma)^{1/2}$: $k_c = 3.4$ (●), $k_c = 4.7$ (▲) and $k_c = 5.7$ (◆). The dashed line is the linear-theory prediction expressed by (2.34).

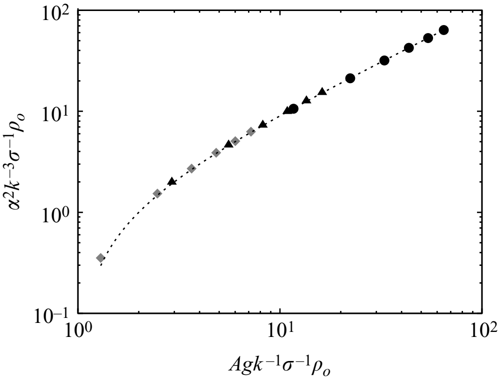

FIGURE 3. The squared growth rate α^2 (see (2.34)) for $k = 1$ (●), $k = 2$ (▲) and $k = 3$ (◆), all smaller than k_c, for six different values of $\mathscr{A}g$ ranging from 0.11 to 0.61. The dashed line corresponds to the linear-theory prediction.

The behaviour of the squared growth rate α^2 (see (2.34)) is shown in dimensionless form in figure 2 as a function of k for three different values of k_c (obtained by varying Ag) and in figure 3 by varying Ag for three different values of $k < k_c$. In both figures, symbols refer to the numerical results and the dashed line is the theoretical expectation given by (2.34).

The numerical data in figures 2 and 3 have been obtained via the best fit of $\langle v^2 \rangle$, the spatial average of v^2 as a function of time. The latter average is computed over a horizontal strip containing the interface (placed in the middle of the computational domain) and having an extension of a_y above and below the interface. This has been done to avoid spurious contamination coming from the upper and lower domain regions affected by the boundary conditions. This is expressed as,

$$\begin{aligned}\langle v^2 \rangle &= \frac{1}{2a_y}\frac{1}{L_x}\int_{-a_y}^{0} \mathrm{d}y \int_0^{L_x} \mathrm{d}x \left(v^{\downarrow}\right)^2 + \frac{1}{2a_y}\frac{1}{L_x}\int_0^{a_y} \mathrm{d}y \int_0^{L_x} \mathrm{d}x \left(v^{\uparrow}\right)^2 \\ &= \frac{1}{2\,a_y\,k}\left[-\mathrm{e}^{-2k\,a_y} + 1\right]\alpha^2 h_0^2 \sinh^2(\alpha\, t), \qquad (3.3)\end{aligned}$$

where we used (2.35) and (2.37) for $v^{\uparrow}$ and $v^{\downarrow}$, respectively.

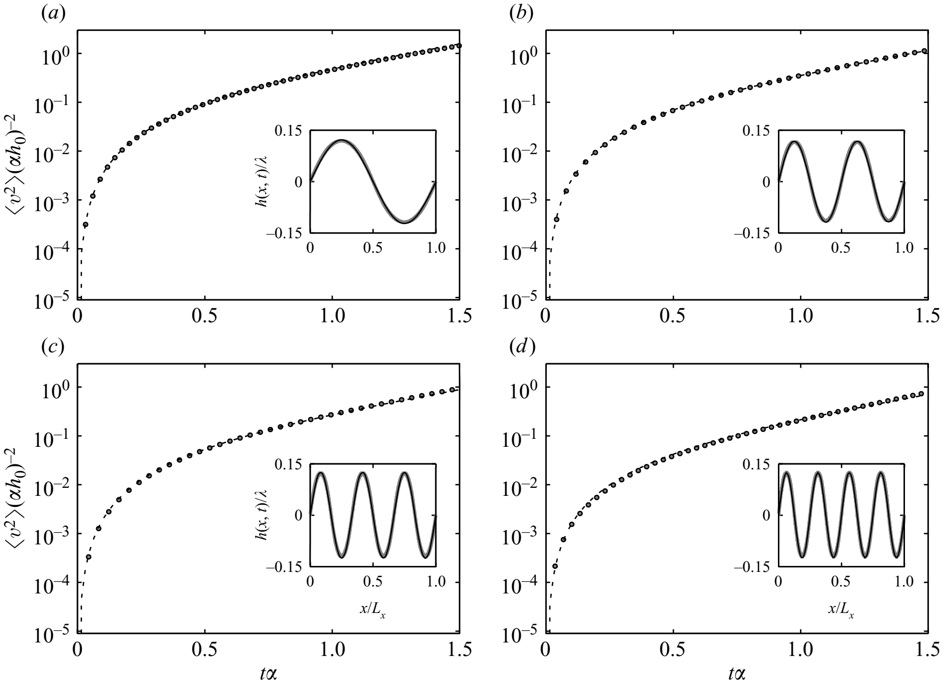

FIGURE 4. Time behaviour of $\langle v^2\rangle$ for $k_c = 4.7$ (in figure 2 corresponding to the solid triangle) and for four values of $k < k_c$. (*a*) $k = 1$, (*b*) $k = 2$, (*c*) $k = 3$ and (*d*) $k = 4$. The numerical results (symbols) are compared with the corresponding best-fit expressions (see the text for details). In the insets, the interface perturbation, $h(x, t)$, is plotted at $t\alpha = 1.5$, revealing a very accurate linear analysis prediction.

The best fit has been done with α as unique free parameter and its high accuracy can be verified in figure 4 where we show the time evolution of $\langle v^2\rangle$ for $k_c = 4.7$ (solid triangles in figure 2) and for four values of k smaller than k_c. At $t\alpha > 1.5$, nonlinear effects start to come into play, giving rise to corrections to the linear analysis (see § 3.4). Up to that time, linear theory is very accurate as we can also see from the insets of figure 4 where the sinusoidal form of $h(x, t)$ is reported for $t\alpha = 1.5$. For testing purposes, for $k = 2$, we have performed a simulation having a computational domain twice (and the same for the resolution along the vertical) the one considered in figure 4. The results are indistinguishable from those in figure 4.

3.2. *Linear instability for finite viscosity*

The aim of this section is to investigate numerically how the growth rate, α appearing in (2.35)–(2.38), is modified by viscosity. As discussed in Appendix B, both an upper and a lower bound for the perturbation growth rate are known (see (B 1) and (B 2)) and we want to assess how the actual growth rates compare with those.

For such a purpose, we choose a surface tension, σ, and $\mathscr{A}g$ in such a way as to obtain instability for a few (unstable) wavenumbers. Our choice was $k_c = 5.7$ (see § 3.1), thus corresponding to five unstable wavenumbers.

As far as the initial perturbation is concerned, we report here the case corresponding to $k = 1$. Initial perturbations with a larger wavenumber simply require an initial smaller amplitude (and eventually a larger numerical resolution) in order to satisfy

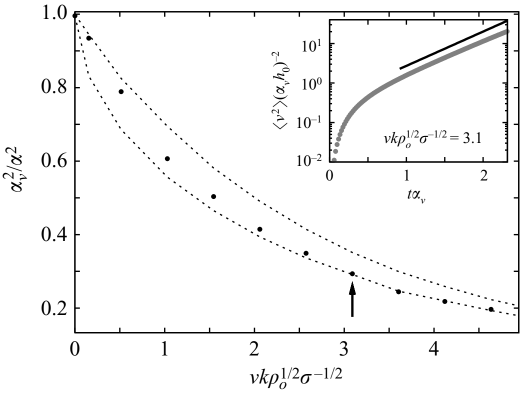

FIGURE 5. Behaviour of the dimensionless perturbation growth rate, α_ν, for $k=1$ and $\mathscr{A}g$ corresponding to $k_c = 5.7$. Dotted lines correspond to upper and lower bounds for the growth rate (see (B 2) and (B 1)). The arrow selects a value of the viscosity for which the time evolution of $\langle v^2\rangle$ is reported in the inset. The continuous line is the best-fit slope (see text).

$h_0 \gg \epsilon$ and $h_0 \ll \lambda$. Here, we have $h_0/\lambda = 0.03$ and $h_0/\epsilon \sim 20$. Such ratios turned out to be sufficiently 'asymptotic' to produce accurate results. The effect of viscosity is studied by considering twelve values of viscosity in the range $10^{-5} \leqslant \nu \leqslant 5\times 10^{-2}$ (model units).

The results of our simulations are summarized in figure 5 where the behaviour of the square perturbation growth rate, α_ν^2, is shown as a function of viscosity. The numerical predictions have been compared with the available theoretical bounds (dashed lines).

Note that the numerical points are always between the two bounds and also how the relative differences between the upper bound and the numerical values are <11 %. This latter fact is compatible, for example, with the results of Menikoff *et al.* (1977).

The values of the growth rates have been obtained via best-fit of $\langle v^2\rangle$ (see (3.3)). Unlike what we did in previous section, here we perform the fit within the exponential region. This is because the non-asymptotic form of the perturbation time evolution is unknown in the present case.

The fit accuracy can be appreciated in the inset of figure 5 where the temporal evolution of the perturbation for $\nu = 0.3$ (model units) is shown together with the best-fit slope (dashed line) from which α_ν is determined. Error bars, estimated by looking at the fit sensitivity by varying the length of the fit interval, are of the order of the symbol sizes.

3.3. *Stable configuration: gravity–capillary waves*

The performance of the phase-field approach in the unstable regime predicted by linear theory both in the presence and in the absence of viscosity proved to be very good. As discussed in § 2.4, for sufficiently large surface tensions and/or sufficiently small differences between fluid densities, a perturbation initially imposed on the fluid interface may maintain its initial amplitude, giving rise to the dispersion relation (2.24). The waves resulting from the balance between gravity and surface tension are known as gravity–capillary waves. Our aim here is to verify their dispersion relation.

To do that, we have fixed the parameters to obtain a critical wavenumber of order one. For $\mathscr{A}g = 0.008$ (model units) and the same σ as in the unstable case,

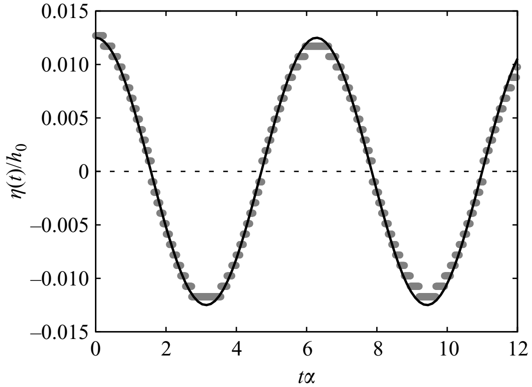

FIGURE 6. Time behaviour of the perturbation maximum, $\eta(t)$, for $k=1$ and $h_0/\lambda=0.012$. The critical wavenumber is $k_c=0.9$. Numerical results (symbols) are compared with the prediction from linear theory.

we have $k_c=0.9$. The first accessible wavenumber is thus stable, and the disturbance should evolve in time according to (2.26). However, the geometrical/computational configuration used in the unstable case did not produce sufficiently accurate results. In particular, using the same domain aspect ratio $L_x/L_y=1$ and the same ratio between perturbation amplitude and perturbation wavelength we found a dynamics too dissipative with respect to what is expected. In the absence of viscosity, dissipation arises in the phase-field formulation owing to the sole contribution proportional to γ in (2.17). The latter parameter has been taken sufficiently small to ensure negligible effects inside a period of oscillation. The specific value was $\gamma=6.25\times10^{-5}$. To avoid spurious dissipation, as that induced by nonlinear effects, we reduced the amplitude of the initial perturbation with respect to the unstable case. Also, we increased the size of the periodicity box along the gravitational direction in such a way as to reduce possible spurious contributions arising from the upper/lower part of the computational domain where instabilities, not present in the unstable case, might now develop. The above choice on the amplitude of the initial perturbation implies a consequent reduction of ϵ. The following set of parameters have been used: $\epsilon=0.008$, $L_x/L_y=1/4$ and a resolution $Nx\times Ny$ of 256×4096. For an initial perturbation on $k=1$, its initial amplitude h_0 has been chosen to have $h_0/\lambda=0.012$ and $h_0/\epsilon\sim10$. The behaviour of the maximum, $\eta(t)$, of the initial perturbation is shown as a function of time in figure 6. The continuous line is relative to a sinusoidal wave with pulsation ω obtained from (2.24). The agreement between theory and numerics is satisfactory, both for the amplitude and for the pulsation. Note the small reduction of $\eta(t)$, in one oscillation period: only 1 grid box over 4096.

3.4. *Weakly nonlinear stage*

In this section, we investigate the early stages of the nonlinear dynamics. We focus on the rising/falling velocity of plumes in the limit of small Atwood numbers when spikes and bubbles are known to coincide. The theoretical prediction for the terminal velocity is reported in Appendix C. Our aim here is both to verify the existence of a regime characterized by a constant ‘terminal’ velocity and, secondly, to compare the prediction (C 1) for such terminal velocity with our numerical data.

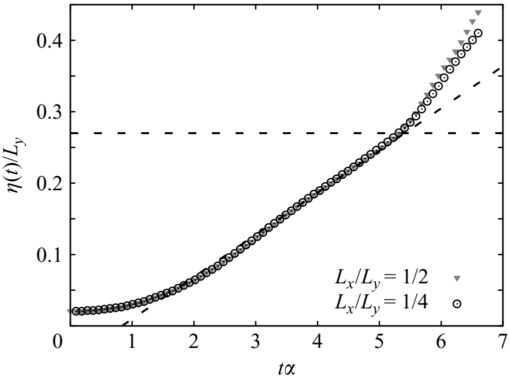

FIGURE 7. Time evolution of amplitude perturbation $\eta(t)$. Symbols are our numerical results for two different domain heights (with the same horizontal extension $L_x = 2\pi$): grey triangles correspond to $L_y = 4\pi$; circles to $L_y = 8\pi$. $\eta(t)$ is made dimensionless with the smallest L_y. Dashed lines are the theoretical slope given by (C 1) and the value $\eta(t)/L_y = 27\,\%$ respectively. Note the agreement between the two numerical results up to $\eta(t)/L_y \sim 27\,\%$.

The physical parameters are chosen to magnify the effect of the surface tension on the terminal velocity. This happens when the wavenumber k of the initial perturbation (still supposed unimodal) is slightly below k_c. Here, we choose $\mathscr{A}g$ and σ such that $k_c = 4.004$, and thus look at the dynamics associated to the wavenumber $k = 3$. The initial perturbation has an amplitude $h_0/\lambda = 0.06$; the initial dynamics is thus linear. Although we are interested in investigating the case of zero viscosity, in order to prevent numerical instabilities we add a small viscosity $\nu = 2 \times 10^{-5}$ (model units). In figure 7, the perturbation amplitude is shown as a function of time: symbols correspond to our numerical data (for two different domain heights) and dashed lines are the theoretical slope given by (C 1) and the value $\eta/L_y = 0.27$, respectively. Good agreement is found between numerics and theory in the range $3 < t\alpha < 5$. At larger times, neighbouring plumes start to interact and the arguments leading to (C 1) no longer apply. Notice also at up to $t\alpha \sim 5$ (corresponding to $\eta/L_y \sim 0.27$), the numerical results obtained with two different domain heights are almost indistinguishable. This is strong evidence of the smallness of the effect of the periodic boundary conditions along the vertical. In figure 8, we show snapshots of the time evolution of the two fluids within the weakly nonlinear stage. Figures are equally spaced in time in the interval $3 < t\alpha < 5$. Black corresponds to $\phi = -1$; white to $\phi = 1$. Their shape is similar to that experimentally observed by Waddell, Niedserhaus & Jacobs (2001). Note the aforementioned spike/bubble symmetry corresponding to the up–down symmetry of our original evolution equations.

4. Conclusions and perspectives

In this paper, we have shown that the phase-field model provides a valuable numerical instrument for the study of immiscible convective hydrodynamics. As a testground for this model, we have considered the Rayleigh–Taylor instability. Numerical results compare very well with known analytical results, both for the linearly stable and unstable cases, and for the weakly nonlinear stages of the latter.

All these results are encouraging in view of the next important step which is the numerical simulations of immiscible RT turbulence. There, the interplay of all the fundamental mechanisms that we have illustrated here (instabilities and wave

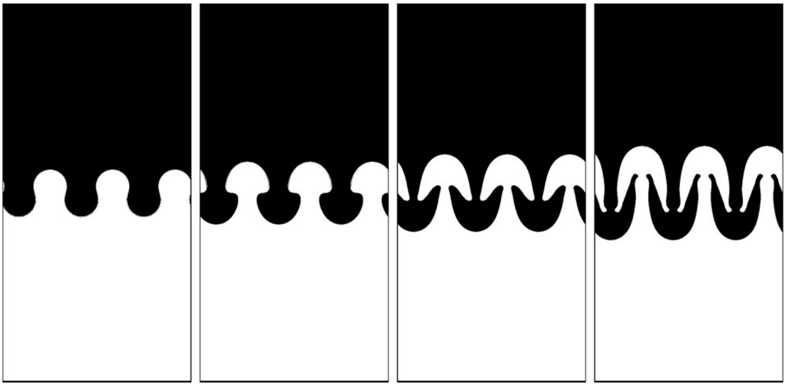

FIGURE 8. A phase-field snapshot: black (white) corresponds to $\phi = -1$ ($\phi = 1$). Frames (corresponding to the domain height $L_y = 4\pi$) are equally spaced in time in the interval $3 < t\alpha < 5$ (see also figure 7).

propagation) is expected to give rise to a small-scale emulsion-like phase dominated by gravity–capillary waves and by a large-scale hydrodynamic range of scales where classical Kolmogorov turbulence should appear. This theoretical suggestion still awaits numerical confirmation, and the phase-field model provides the appropriate method for pursuing this goal.

We acknowledge useful discussions with Hekki Haario. A. M. and L. V. have been partially supported by PRIN 2005 project 2005027808 and by CINFAI consortium (A. M.). L. V. acknowledges support from 'From Discrete to Continuous models for Multiphase Flows' TEKES project 40289/05.

Appendix A. Details on the dispersion relation for the phase-field model

Let us start our analysis from (2.18) for the phase field ϕ:

$$\phi = f\left(\frac{y - h(x,t)}{\epsilon}\right), \tag{A 1}$$

where, we recall that h can be larger than ϵ, yet it must be smaller than the scale of variation of h (small amplitudes).

From the condition of local equilibrium of the interface we find

$$f'' = V'(f), \tag{A 2}$$

where $V(\phi) = (\phi^2 - 1)^2/4\epsilon^2$. Under the above conditions, the following expression for the chemical potential μ is:

$$\mu = -\Lambda \frac{\partial^2 f}{\partial x^2} = \frac{\Lambda}{\epsilon}\left[f' \frac{\partial^2 h}{\partial x^2} - \frac{f''}{\epsilon}\left(\frac{\partial h}{\partial x}\right)^2\right]. \tag{A 3}$$

Linearizing (2.6) for small interface velocity we have, neglecting the viscous term:

$$\rho_o \partial_t v = -\partial_y p - \phi \partial_y \mu - \mathscr{A} g \rho_o \phi. \tag{A 4}$$

The integration of (A 4) in the vertical direction, interpreted in the principal value sense,

$$q_y \equiv \lim_{L\uparrow\infty} \int_{-L}^{L} v \,\mathrm{d}y, \tag{A 5}$$

$$\rho_o \partial_t q_y \equiv \lim_{L\uparrow\infty} \left\{ \frac{\Lambda}{\epsilon} \int_{-L}^{L} \left[f f'' \frac{\partial^2 h}{\partial x^2} - \frac{1}{\epsilon} f f''' \left(\frac{\partial h}{\partial x} \right)^2 \right] \mathrm{d}(y/\epsilon) - \mathscr{A} g \rho_o \int_{-L}^{L} f \,\mathrm{d}y \right\}, \tag{A 6}$$

yields:

$$\rho_o \partial_t q_y = \sigma \frac{\partial^2 h}{\partial x^2} - 2\mathscr{A} g \rho_o h, \tag{A 7}$$

having used the relations $\int (f')^2 \,\mathrm{d}y = 2\sqrt{2}/3$, $\int f f''' \,\mathrm{d}y = 0$ and

$$\lim_{L\uparrow\infty} \int_{-L}^{+L} f \,\mathrm{d}y = +2h. \tag{A 8}$$

The height variation of the interface has to match the vertical fluid velocity, thus giving:

$$\partial_t h = v(x, h(x,t), t) \equiv v^{(int)}(x,t). \tag{A 9}$$

The last step is to relate the velocity at the interface with the integral q_y. This is done by restricting ourselves to potential flows:

$$\boldsymbol{v} = \boldsymbol{\partial} \psi, \qquad \partial^2 \psi = 0. \tag{A 10}$$

For $y > 0$, with '$\hat{}$' denoting the Fourier transform, we have:

$$\psi(x,y,t) = \int_0^\infty \mathrm{e}^{-ky+\mathrm{i}kx} \hat{\psi}(k,t) \,\mathrm{d}k + \text{c.c.} \tag{A 11}$$

$$v(x,y,t) = -\int_0^\infty k \mathrm{e}^{-ky+\mathrm{i}kx} \hat{\psi}(k,t) \,\mathrm{d}k + \text{c.c.} \tag{A 12}$$

$$q_y(x,t) = -2 \int_0^\infty \mathrm{e}^{\mathrm{i}kx} \hat{\psi}(k,t) \,\mathrm{d}k + \text{c.c.} \tag{A 13}$$

$$v^{(int)} = -\int_0^\infty k \mathrm{e}^{\mathrm{i}kx} \hat{\psi}(k,t) \,\mathrm{d}k + \text{c.c.} \tag{A 14}$$

Therefore:

$$\hat{v}^{(int)} = (k \hat{q}_y)/2, \tag{A 15}$$

so that in k-space we have:

$$\partial_t \hat{h} = (k \hat{q}_y)/2, \qquad \rho_o \partial_t \hat{q}_y = (-\sigma k^2 - 2\mathscr{A} g \rho_o) \hat{h}. \tag{A 16}$$

From these two equations, we immediately obtain:

$$\partial_t^2 \hat{h} + \omega^2 \hat{h} = 0, \tag{A 17}$$

with:

$$\omega^2(k) = \mathscr{A} g k + \frac{\sigma}{2\rho_o} k^3, \tag{A 18}$$

which is the expected dispersion relation (Chandrasekhar 1961).

Appendix B. Bounds for the perturbation growth rate in the presence of viscosity

The effect of viscosity is to reduce the perturbation growth rate. However, it does not remove the instabilities. Analytically, it is more difficult to consider the effect of viscosity with respect to surface tension (see (115) of Chandrasekhar 1961, p. 443). Nonetheless, it is possible to determine a lower and an upper bound to the growth rate α_ν. These bounds are the solutions to the following equations (Menikoff *et al.* 1977):

$$\alpha_\nu^4 + 2\nu k^2 \alpha_\nu^3 + \left(\nu^2 k^3 - \frac{\alpha^2}{k}\right) k \alpha_\nu^2 - \left(\nu^2 k^3 + \frac{\alpha^2}{k}\right) \nu k^3 \alpha_\nu - \left(\nu^4 k^6 - \frac{\alpha^4}{k^2}\right) k^3 = 0, \tag{B 1}$$

$$\alpha_\nu^2 + 2\nu k^2 \alpha_\nu - \alpha^2 = 0, \tag{B 2}$$

where α is the growth rate in the inviscid case (see (2.34)). The solution of (B 2) is:

$$\alpha_\nu = -k^2\nu + \sqrt{k^4\nu^2 + \alpha^2}, \tag{B 3}$$

while only a numerical solution is available for (B 1).

The goodness of those upper and lower bounds are numerically investigated in § 3.2 by means of the phase-field model.

Appendix C. Models for the terminal bubbles/spike velocities in the weekly nonlinear regime

Substantial deviations from the linear theory are observed when the perturbation amplitude reaches a size of the order of $0.1\,\lambda$ – $0.4\,\lambda$ (Sharp 1984).

In that case, the disturbance grows nonlinearly and the interface starts to deform. Indeed, at least for finite values of $\mathscr{A}$, the interface can be divided into spikes corresponding to the regions where the heavier fluid penetrates into the lighter one, and bubbles associated to those regions where lighter fluid rises in the heavier one. The roll-up of vortices produces a mushroom-type shape for bubbles and spikes (see, e.g. Waddell *et al.* 2001). When the fluid densities are similar (corresponding to our case $\mathscr{A} \ll 1$), spikes and bubbles coincide and approach a constant and equal velocity. In both cases, the exponential growth of the velocity perturbation amplitude characterizing the linear phase of the evolution is replaced by a linear-in-time behaviour (Waddell *et al.* 2001). Two models are available to describe this stage: the drag-buoyancy model (Alon *et al.* 1995) and the 'Layzer model' (Layzer 1955; Goncharov 2003; Young & Ham 2006). The former model describes bubble and spike motion by balancing the buoyancy and drag forces and it assumes that these velocities reach constant values for sufficiently long times. The latter model uses an expansion of the perturbation amplitudes and conservation equations near the tip of the bubbles and spikes. This approach was first applied to the fluid–vacuum interface ($\mathscr{A} = 1$) (Layzer 1955), and then extended to arbitrary Atwood numbers (Goncharov 2003) and to include the surface-tension contribution (Young & Ham 2006). According to the latter study, in our case (bidimensional flow, immiscible fluids and small Atwood number), we expect that the terminal bubble and spike velocity can be obtained from the results of Young & Ham (2006):

$$U(t \to \infty) = \sqrt{\frac{2}{3}\mathscr{A}\frac{g}{k} - \frac{2}{9}\frac{\sigma}{\rho_2 + \rho_1}k}. \tag{C 1}$$

This expectation is numerically tested, in § 3.4, by exploiting the phase-field method.

REFERENCES

Alon, U., Hecht, J., Ofer, D. & Shvarts, D. 1995 Power laws and similarity of Rayleigh–Taylor and Richtmyer–Meshkov mixing fronts at all density ratio. *Phys. Rev. Lett.* **74**(4), 534–537.

Anderson, D. M., McFadden, G. B. & Wheeler, A. A. 1998 Diffuse-interface methods in fluid mechanics. *Annu. Rev. Fluid Mech.* **30**, 139–165.

Badalassi, V. E., Ceniceros H. D. & Banerjee, S. 2003 Computation of multiphase systems with phase field models. *J. Comput. Phys.* **190**, 371–397.

Berti, S., Boffetta, G., Cencini, M. & Vulpiani, A. 2005 Turbulence and coarsening in active and passive binary mixtures. *Phys. Rev. Lett.* **95**, 224501-1–224501-4.

Bray, A. J. 2002 Theory of phase-ordering kinetics. *Adv. Phys.* **51**, 481–587.

Cabot, W. H. & Cook, A. W. 2006 Reynolds number effects on Rayleigh–Taylor instability with possible implications for type-Ia supernovae. *Nature phys.* **2**, 562–568.

Cahn, J. W. & Hilliard, J. E. 1958 Free energy of a non uniform system. I. Interfacial free energy. *J. Chem. Phys.* **28**, 258–267.

Canuto, C., Hussaini, M. Y., Quarteroni, A. & Zang, T. A. 1988 *Spectral Methods in Fluid Dynamics.* Series in Computational Physics. Springer.

Celani, A., Mazzino, A. & Vozella, L. 2006 Rayleigh–Taylor turbulence in two-dimensions. *Phys. Rev. Lett.* **96**, 134504-1–134504-4.

Chandrasekhar, S. 1961 *Hydrodynamic and Hydromagnetic Stability.* Dover.

Chertkov, M. 2003 Phenomenology of Rayleigh–Taylor turbulence. *Phys. Rev. Lett.* **91**, 115001-1–115001-4.

Chertkov, M., Kolokolov, I. & Lebedev, V. 2005 Effects of surface tension on immiscible Rayleigh–Taylor turbulence. *Phys. Rev.* E **71**, 055301-1–055301-4.

Cook, A. W. & Zhou, Y. 2002 Energy transfer in Rayleigh–Taylor instability. *Phys. Rev.* E **66**, 026312-1–026312-12.

Dimonte, G. & Schneider, M. 2000 Density ratio dependence of Rayleigh–Taylor mixing for sustained and impulsive acceleration histories. *Phys. Fluids* **12**, 304–321.

Ding, H., Spelt, P. D. M. & Shu, C. 2007 Diffuse interface model for incompressible two-phase flows with large density ratios. *J. Comput. Phys.* **226**, 2078–2095.

Di Prima, R. C. & Swinney, H. L. 1981 *Hydrodynamic Instabilities and the Transition to Turbulence.* (ed. H. L. Swinney & J. P. Gollup) Springer.

Ducea, M. & Saleeby, J 1998 A case for delamination of the deep batholithic crust beneath the Sierra Nevada, California. *Intl Geol. Rev.* **40**, 78–93.

Goncharov, V. N. 2003 Analytical model of nonlinear, single-mode, classical Rayleigh–Taylor instability at arbitrary Atwood numbers. *Phys. Rev. Lett.* **88**, 134502-2–134502-4.

Kull, H. J. 1991 Theory of the Rayleigh–Taylor instability. *Phys. Rep.* **206** (5), 197–325.

Kundu, P. K. & Cohen, I. M. 2001 *Fluids Mechanics*, 2nd edn. Academic.

Jacqmin, D. 1999 Calculation of two-phase Navier–Stokes flows using phase-field modeling. *J. Comput. Phys.* **155**, 96–127.

Landau, L. D. & Lifshitz, E. M. 2000 *Fluid Mechanics. Course of Theoretical Physics.* 2nd edn, Revised. Butterworth–Heinemann.

Layzer, D. 1955 On the instability of superposed fluids in a gravitational field. *Astrophys. J.* **122**, 1–12.

Lee, C.-T., Rudnick, R. L. & Brimhall Jr, G. H. 2001 Deep lithospheric dynamics beneath the Sierra Nevada during the Mesozoic and Cenozoic as inferred from xenolith petrology. *Geochem. Geophys. Geosys.* **2**, 2001GC000152.

Liu, C. & Shen, J. 2003 A phase field model for the mixture of two incompressible fluids and its approximation by a Fourier-spectral method. *Physica* D **179**, 211–228.

Menikoff, R., Mjolsness, R. C., Sharp, D. H. & Zemach, C. 1977 Unstable normal mode for Rayleigh–Taylor instability in viscous fluids. *Phys. Fluids* **20** (12), 2000–2004.

Ramabrabhu, P. & Andrews, M. J. 2004 Experimental investigation of Rayleigh–Taylor mixing at small Atwood numbers. *J. Fluid Mech.* **502**, 233–271.

Rayleigh, Lord 1883 Investigation of the character of the equilibrium of an incompressible heavy fluid of variable density. *Proc. Lond. Math. Soc.* **14**, 170–177.

Schultz, D. M., Kanak, K. M., Straka, J. M., Trapp, R. J., Gordon, B. A., Zrnić, D. S., Bryan, G. H., Durant, A. J., Garrett, T. J., Klein, P. K. & Lilly, D. K. 2006 The mysteries of Mammatus clouds: observations and formation mechanisms. *J. Atmos. Sci.* **10**, 2409–2435.

Sethian, A. J. 1999 *Level Set Methods and Fast Marching Methods: Evolving Interfaces in Computational Geometry, Fluid Mechanics, Computer Vision and Materials Science.* Cambridge University Press.

Sharp, D. H. 1984 An overview of Rayleigh–Taylor instability. *Physica* D **12**, 3–18.

Smolianski, A., Haario, H. & Luukka, P. 2005 Vortex shedding behind a rising bubble and two-bubble coalescence: a numerical approach. *Appl. Math. Model* **29**, 615–632.

Taylor, G. I. 1950 The instability of liquid surfaces when accelerated in a direction perpendicular to their planes I. *Proc. R. Soc. Lond.* A **201**, 192–197.

Waddell, J. T., Niederhaus, C. E. & Jacobs, J. W. 2001 Experimental study of Rayleigh–Taylor instability: low Atwood number systems with single-mode initial perturbations. *Phys. Fluids* **13** (5), 1263–1273.

Young, Y. N. & Ham, F. E. 2006 Surface tension in incompressible Rayleigh–Taylor mixing flow. *J. Turbulence.* **71** (7), 1–23.

Young, Y. N., Tufo, H., Dubey, A. & Rosner, R. 2001 On the miscible Rayleigh–Taylor instability: two and three dimensions. *J. Fluid Mech.* **447**, 377–408.

Yue, P., Feng, J. J., Liu, C. & Shen, J. 2004 A diffuse-interface method for simulating two-phase flows of complex fluids. *J. Fluid Mech.* **515**, 293–317.